

High-Q 2D Lithium Niobate Photonic Crystal Slab Nanoresonators

Mingxiao Li, Hanxiao Liang, Rui Luo, Yang He, and Qiang Lin*

Lithium niobate (LN), known as the “silicon of photonics,” exhibits outstanding material characteristics with great potential for broad applications. Enhancing light–matter interaction on the nanoscale would result in intriguing device characteristics that enable new physical phenomena to be revealed and novel functionalities inaccessible by conventional means to be realized. High-Q 2D photonic crystal (PhC) slab nanoresonators are particularly suitable for this purpose, which, however, remains an open challenge to be realized on the lithium niobate platform. Here, an important step is taken toward this direction, demonstrating 2D LN PhC slab nanoresonators with optical Q as high as 3.51×10^5 , about three orders of magnitude higher than other 2D LN PhC structures reported to date. The high optical quality, tight mode confinement, together with specific polarization characteristics of the devices enable the peculiar anisotropy of photorefractive quenching and unique anisotropic thermo-optic nonlinear response to be revealed. They also allow the observation of third-harmonic generation in on-chip LN nanophotonic devices, and a strong orientation-dependent generation of the second harmonic.

1. Introduction

Photonic crystal (PhC) nanoresonators exhibit exceptional capability of controlling light confinement and light–matter interactions in the sub-wavelength scale, which forms a crucial foundation for many applications such as signal processing,^[1] information storage,^[2] bio-sensing,^[3] nonlinear photonics,^[4] cavity quantum electrodynamics,^[5] among many others. Among various photonic crystal structures, 2D photonic crystal slabs exhibit significant advantage in the engineering of the density of photonic states, the flexibility of device structure design, the scalability of optoelectronic integration, and the compatibility with current nanofabrication technology. These excellent characteristics have excited tremendous interest in recent years to develop 2D PhC slab nanoresonators on a variety of material platforms.^[1–11]

Lithium niobate (LN), known as “silicon of photonics,”^[12] exhibits outstanding electro-optic, nonlinear optical, acousto-optic, piezoelectric, photorefractive, pyroelectric, and photoconductive properties,^[13] promising for broad applications.^[14] The great application potential has attracted significant attention recently to develop LN photonic devices on chip-scale platforms.^[15–36] However, realizing high-quality 2D LN PhC structures remains significant challenge,^[37–47] which becomes the major obstacle hindering the exploration of optical phenomena in the nanoscopic scale that would potentially result in intriguing device characteristics and novel functionalities inaccessible by conventional means.

Herein, we demonstrate 2D LN PhC slab nanoresonators with optical Q up to 3.51×10^5 , about three orders of magnitude higher than other 2D LN photonic crystal nanocavities reported to date.^[37–47] The high optical Q together with the tiny effective mode volume supports extremely strong nonlinear optical interactions, which results in interesting third-harmonic generation in on-chip LN nanophotonic devices.^[15–36] In particular, the specific polarization characteristics of the cavity modes enabled us to reveal peculiar anisotropy of photorefractive quenching and unique anisotropic thermo-optic nonlinear response. It also allowed us to observe strong orientation-dependent generation of the second harmonic. The demonstrated high-Q 2D LN PhC nanoresonators not only offer an excellent device platform for the exploration of extreme nonlinear and quantum optics at single-photon and few-photon level, but also open up a great avenue toward future development of energy efficient nonlinear photonic and electro-optic signal processing.

2. Device Design and Fabrication

The major challenge in making high quality 2D LN photonic crystal structure lies in the complexity of device structures and the stringent requirement on fabrication precision which are significantly beyond current technology to define LN nanophotonic structures. For example, current plasma etching approaches generally produce a slant angle on the device sidewall.^[18,24] Although such a slant angle can be incorporated into the design of 1D LN photonic crystal,^[32] it imposes serious challenge in both the

Dr. M. Li, Dr. H. Liang, Dr. Y. He, Prof. Q. Lin
Department of Electrical and Computer Engineering
University of Rochester
Rochester, NY 14627, USA
E-mail: qiang.lin@rochester.edu
Dr. R. Luo, Prof. Q. Lin
Institute of Optics
University of Rochester
Rochester, NY 14627, USA

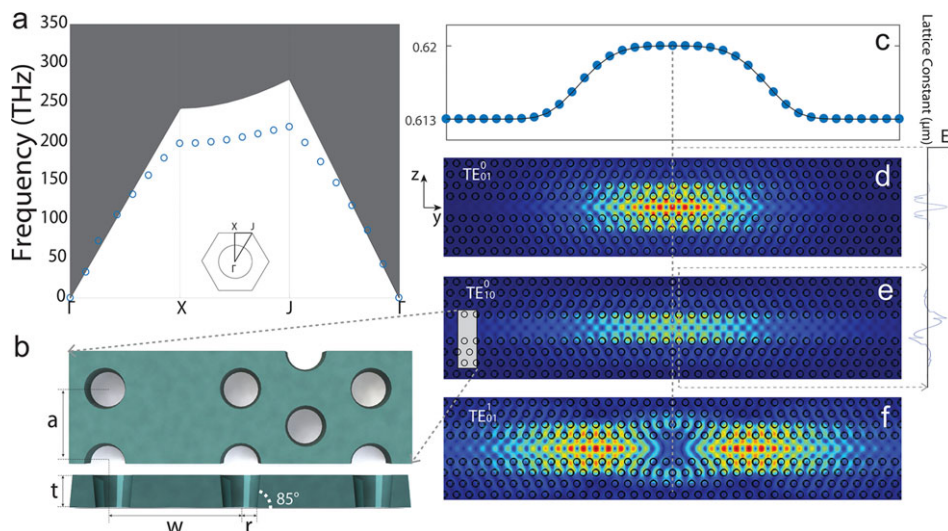


Figure 1. Properties of the photonic band structure and line-defect cavity modes of the designed 2D LN photonic crystal slab. a) Dispersion property of the fundamental transverse-electric-like (TE-like) guided mode inside the designed 2D photonic crystal slab. b) Schematics showing the top view and cross section of the 2D PhC slab with a line defect waveguide. c) Lattice constant as a function of position, which is optimized for high radiation-limited optical Q. d–f) The optical mode field profiles of the fundamental (TE_{01}^0 and TE_{10}^0) and second-order (TE_{01}^1) TE cavity modes, with electric field dominantly lying in the device plane. The mode field profiles are simulated by the finite element method. The left inset shows the orientation of crystal where the optical axis is along the z direction. The right inset shows the E_z cavity fields as a function of transverse position, at the cross sections indicated by the dashed lines.

design and fabrication of 2D structures which has much more stringent requirement on the sidewall verticality. On the other hand, LN is a ferroelectric crystal with strong material anisotropy, which leads to significant etching anisotropy in the device plane, making it challenging to define nanoscopic circular hole structures required by 2D photonic crystals.^[37–47]

We overcame all these challenges by optimizing the fabrication processes, which were able to produce a sidewall angle of about 85° uniformly across the whole device structure (Figures 1 and 2). Such a nearly vertical device sidewall enabled us to design well-defined photonic guided modes, as shown in Figure 1a. We optimized the layer thickness t , hole radius r , and lattice constant a of a hexagonal structure to enlarge the photonic bandgap. Detailed simulations by the finite element method shows that a layer thickness of 270 nm, a hole radius of 145 nm, together with a lattice constant of 620 nm is able to achieve an optimized bandgap of 28.1 THz in the telecom band, with the fundamental transverse-electric (TE) polarized guided mode well confined below the light line (Figure 1a).

To produce a well-confined line-defect cavity, we employed the multi-heterostructure design,^[6] by gradually varying the lattice constant from 620 to 613 nm around the center of the line-defect waveguide (Figure 1b,c) and optimizing the waveguide width w to minimize the radiation leakage. Figure 1d–e show the simulated optical mode field profiles of the fundamental (TE_{01}^0 and TE_{10}^0) and second-order (TE_{01}^1) TE-like cavity modes, which exhibit radiation-limited optical Qs of 1.5×10^6 , 5×10^5 , and 3×10^5 , respectively, with effective mode volumes of $2.43(\lambda/n)^3$, $3.06(\lambda/n)^3$, and $4.63(\lambda/n)^3$. In particular, the nearly vertical device sidewalls here significantly decrease the polarization hybridization, in contrast to the 1D photonic crystal nanobeams demonstrated recently.^[32] For example, the fundamental cavity mode TE_{01}^0 shown in Figure 1d exhibits 62.5% of its energy in

the z-polarization lying in the device plane, almost zero in the x-direction, and about 37.5% in the y-direction. The significant dominance of polarization along one direction enables us to explore intriguing anisotropy of optical phenomena, by making the line-defect cavity either in parallel with or perpendicular to the optical axis, as we will show below. For convenience, we denote the one perpendicular to the optical axis as an e-cavity since the dominant electric field polarizes along the optical axis, corresponding to the extraordinary polarization (see Figure 1d). Accordingly, we denote the one in parallel with the optical axis as an o-cavity as the dominant cavity field polarizes along the ordinary polarization.

Our devices were fabricated on a 270-nm-thick X-cut single-crystalline LN thin film sitting on a 2-μm silicon dioxide layer on a silicon substrate. To define the photonic crystal structure, we deposited first a 400-nm thick amorphous silicon as a hard-etching mask through plasma enhanced chemical vapor deposition. The device structure was patterned with ZEP-520A positive resist via electron-beam lithography, which was then transferred to the amorphous silicon mask layer with a standard reactive ion etching process. It was in turn transferred to the LN layer with an Ar^+ plasma etching process. The residual mask was removed by a 30% KOH resolvent at 70 °C. Finally, we use diluted hydrofluoric acid to undercut the buried oxide layer to form a suspended photonic crystal membrane structure (Figure 2a,b).

3. Optical Properties

Figure 2a,b show an example of a fabricated device. It shows clearly that we achieved a nearly vertical device sidewall both inside and outside the circular holes, uniformly across the entire device structure. The circular shape of holes is well defined and the hexagonal lattice structures is accurately patterned. To characterize the optical property of the device, we launched a

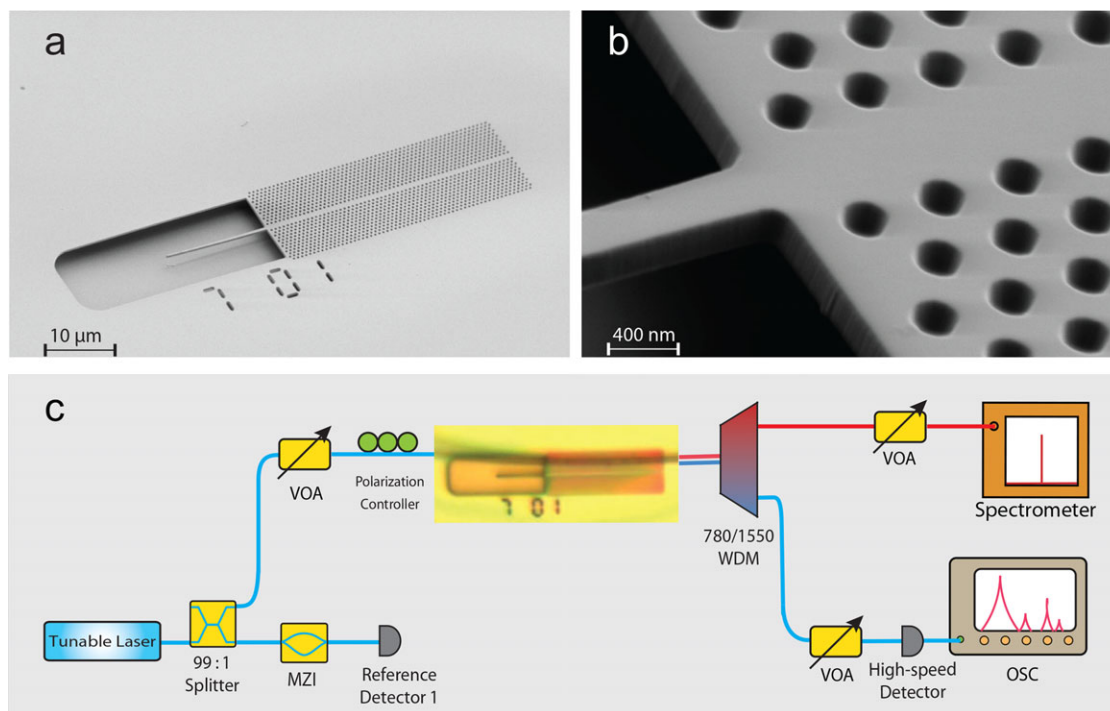


Figure 2. Fabricated device structure and experimental testing setup. a) Scanning electron microscopy image of a fabricated 2D LN PhC slab. b) Zoom-in image of a section of the photonic crystal slab. c) Schematic of the experimental testing setup. MZI, Mach–Zehnder interferometer, used to calibrate the laser wavelength; VOA, variable optical attenuator; WDM, wavelength-division multiplexed filter; OSC, oscilloscope. The inset shows an optical microscopy image of a device side coupled to a tapered optical fiber.

continuous-wave tunable laser into the device via evanescent side-coupling with a tapered optical fiber. Figure 2c shows the schematic of the experimental testing setup, where the optical wave transmitted out from the device is detected by a photodetector whose output is characterized by an oscilloscope. In the case of harmonic generation, the harmonic light was separated by a dichroic filter and then recorded by a spectrometer.

Figure 3a shows the transmission spectrum of an e-cavity device recorded when we scanned the laser over a telecom band. It shows that the devices exhibit five cavity modes located at two spectral regions between 1535 and 1541 nm and between 1572 and 1582 nm, with the mode species identified on the figure. Detailed characterizations (Figure 3b,c) show that the fundamental cavity mode TE_{01}^0 located at 1578.96 nm exhibits an intrinsic optical Q as high as 3.34×10^5 , while the second-order mode TE_{10}^0 at 1539.36 nm has an optical Q about one order of magnitude lower. The o-cavity devices exhibit the same magnitude of optical quality. One example is shown in Figure 3d, which shows an optical Q of 3.51×10^5 that is even higher than that of the e-cavity. These optical Qs are about three orders of magnitude higher than other 2D LN photonic crystal nanocavities reported to date.^[37–47] They are only about five times lower than the theoretically designed values, indicating the high quality of device fabrication.

To obtain the dependence of optical Q on the width of line-defect waveguide, we characterized more than 50 e-cavity nanoresonators with varied waveguide width. Figure 3e shows the results for the TE_{01}^0 mode. It shows clearly that the experimentally recorded optical Q maintains above 1.5×10^5 for a large range of waveguide width between 1.10 and 1.33 μm , with a peak

value appearing at $w = 1.27 \mu\text{m}$. This trend agrees well with the numerical simulations shown in the solid line. The o-cavities exhibit similar dependence on the waveguide width, while the waveguide width leading to the peak optical Q shifts to $w = 1.18 \mu\text{m}$, simply due to the birefringence of LN crystal.

4. Photorefraction

The high quality and the small effective mode volume of the 2D LN photonic crystal slab nanoresonators would result in dramatic enhancement of optical energy density inside the cavity, which would thus support strong nonlinear optical interaction. In particular, the polarization characteristics of the cavity modes in these devices enables us to explore the potential anisotropy of nonlinear optical phenomena. This anisotropy is challenging to access in 1D LN photonic crystal nanobeams^[32] that exhibit significant polarization hybridization due to the specific shape of the device cross section. In the following, we explore photorefractive effect, thermo-optic bistability, and harmonic generation, which show intriguing behaviors in the nanoscopic scale that do not appear in any other LN photonic devices.

To do so, we selected an e-cavity and an o-cavity with the same intrinsic optical Q of 3.3×10^5 for the fundamental TE_{01}^0 cavity mode. For a fair comparison between the two devices, we maintained exactly same operation conditions for the two devices, by positioning the coupling tapered fiber to maintain a same external coupling efficiency of 70% for both devices (accordingly, same loaded optical Q around 2.1×10^5 for both cavities). To explore the photorefractive effect, we increased the input optical power to

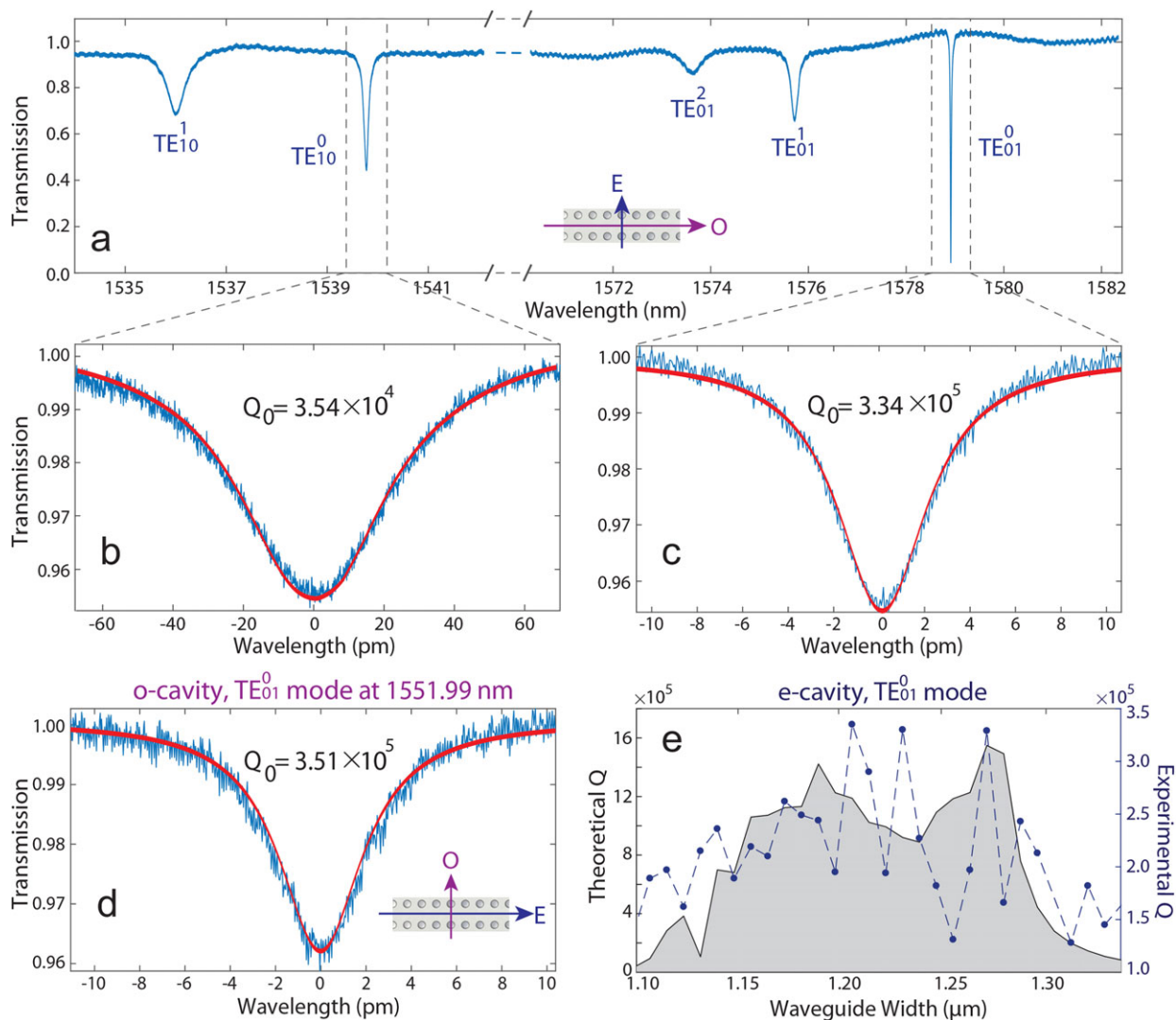


Figure 3. Linear optical properties of 2D LN PhC slab nanoresonators. a) Laser-scanned transmission spectrum of an e-cavity. The inset shows the top-view schematic of the e-cavity device orientation with respect to the optical axes. b,c) Detailed transmission spectra of the TE_{10}^0 and TE_{01}^0 cavity modes, respectively, with the experimental data shown in blue and the theoretical fitting shown in red. d) Detailed transmission spectrum of the fundamental TE_{01}^0 cavity mode in an o-cavity, with the experimental data shown in blue and the theoretical fitting shown in red. The inset shows the top-view schematic of the o-cavity device orientation. e) Optical Qs of the TE_{01}^0 mode in e-cavities as a function of the width of line-defect waveguide. The blue dots show the experimental data and the solid line shows the theoretical results simulated by the finite element method. The fluctuations on the theoretical curve are primarily due to the precision of numeric simulations, which is limited by the finite size of the computer memory. The dashed line is used for eye guidance only.

2 mW, at which the photorefractive is quenched in both devices, an intriguing phenomena we also observed previously in the 1D LN photonic crystal nanobeams.^[32] We maintained the devices at this condition for about 15 min to stabilize the photorefractive quenching. After that, we varied the optical power and monitored the transmission of the devices when we continuously scanned the laser wavelength across the cavity resonances back and forth in a periodic triangular fashion.

Figure 4 shows the laser-scanned transmission spectra of the cavities at different optical power levels. The quenching of photorefractive behaves very differently in the two cavities. In the e-cavity, Figure 4a shows that the left edge of the cavity resonance remains unchanged when the input power is varied be-

tween the whole range from 2 μW to 0.8 mW, as indicated by the dashed line. Since the left edge of the cavity resonance indicates the spectral location of the passive cavity (in the absence of optical wave), this implies a complete quenching of the photorefractive. In the o-cavity, surprisingly, Figure 4b shows that the left edge of the cavity resonance shifts toward red when the input power increases from 0.08 to 0.32 mW, as indicated by the red dashed line. However, it shifts backward toward blue when the optical power increases further from 0.32 to 0.8 mW, as indicated by the blue dashed line. The whole process is reversible when the optical power changes. To the best of our knowledge, this is the first time to observe such peculiar anisotropic behavior of photorefractive quenching. The underlying mechanism is

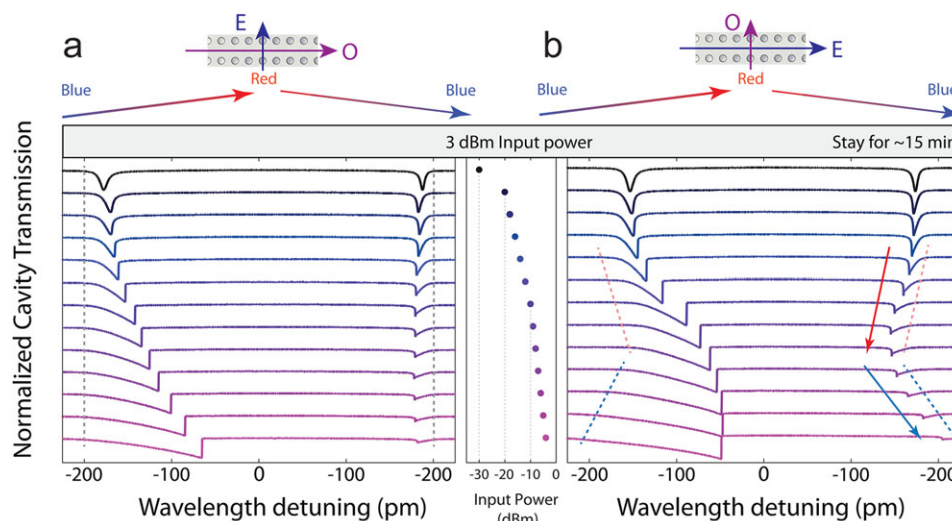


Figure 4. Laser-scanned cavity transmission spectrum as a function of input power. The input optical power remains first at 2 mW for about 15 min (gray region) to quench the photorefractive before we started recording the transmission spectra at different power levels. The input power corresponding to each scanning spectrum is shown in the middle. The laser wavelength is periodically scanned back and forth in a triangular fashion over a spectral range of 230 pm, with a scanning period of 100 ms. The cavity transmission spectra are shifted with each other along the vertical axis for convenient comparison. a) The left panel is recorded for an e-cavity (indicated on the top), where the dashed line indicates the left edge of the cavity resonance which remains unchanged with optical power. b) The right panel is for an o-cavity, where the red and blue dashed lines show the red and blue shifts, respectively, of the left edge of the cavity resonance.

not clear at this moment. One potential reason is likely related to the photovoltaic property of lithium niobate, which tends to produce photocurrent preferably along certain crystallographic axis.^[13] However, the exact physical nature requires further exploration in the future.

5. Thermo-Optic Nonlinearity

Figure 4a,b show clear thermo-optic bistability when the input optical power becomes significant, as expected. However, it is interesting to note that, at a same power level, the thermo-optic bistability in the o-cavity is considerably larger than that in the e-cavity. This is surprising since the two devices exhibit identical intrinsic optical Q and operates with exactly same external coupling condition, from which we expect a same temperature change due to photothermal heating. As the thermo-optic coefficient for the extraordinary polarization ($\frac{dn_e}{dT} = 3.34 \times 10^{-5} \text{ K}^{-1}$) is significantly greater than that for the ordinary light ($\frac{dn_o}{dT} = 0 \text{ K}^{-1}$) at room temperature in the telecom band, and the thermal expansion along the optical axis ($\alpha^{(z)} = 0.75 \times 10^{-5} \text{ K}^{-1}$) is only slightly smaller than that along the orthogonal direction ($\alpha^{(x,y)} = 1.54 \times 10^{-5} \text{ K}^{-1}$), we shall expect a larger thermo-optic bistability in the e-cavity instead.

The peculiar thermo-optic nonlinear behavior is likely due to the pyroelectricity of lithium niobate,^[13] which produces an electric field along the crystal axis when temperature increases. The induced electric field in turn decreases the refractive index via the Pockels effect, which compensates the refractive index increase induced by the thermo-optic effect. As the Pockels effect is dominant along the optical axis, the e-cavity will experience more the pyroelectricity-induced refractive index change, leading to a smaller net increase of refractive index. Note that the time re-

sponse of the pyroelectricity is primarily determined by that of the temperature variation which is the same as a normal thermo-optic effect. Consequently, the combined thermo-optic nonlinearity and the pyroelectricity-induced effect would manifest as a net thermo-optic bistability, which is smaller in an e-cavity than an o-cavity, as we observed in Figure 4.

6. Harmonic Generation

Lithium niobate exhibits significant second-order optical nonlinearity. Therefore, the strong nonlinear optical interactions in the 2D LN PhC slab nanoresonators would enable us to observe second-harmonic generation (SHG). **Figure 5** shows an example. When we increased the optical power dropped into the e-cavity, a bright spot appeared at the center of the device structure where the nanoresonator is located, which is clearly visible in the optical microscopic image (Figure 5a). As the imaging camera has a spectral response in the visible and near infrared, the bright spot implies the generation of the second harmonic. This is verified by the emission spectrum shown in Figure 5c which shows a clear coherent emission line at 778.73 nm when we launched a pump wave into the cavity mode at 1557.45 nm. The SHG exhibits a quadratic power dependence, as shown in Figure 5d, which is a typical signature of second-harmonic generation. Figure 5d shows a conversion efficiency of 0.078 \%W^{-1} . The small value is primarily due to the SHG frequency which is well above the light line of the 2D photonic crystal (Figure 1a) that was designed only for high-Q cavities in the telecom band, leading to low optical Q around the second harmonic with significant radiation leakage into free space. On the other hand, the coupling tapered optical fiber was designed for operating in the telecom band, which exhibits very low coupling efficiency at shorter waveband. Future

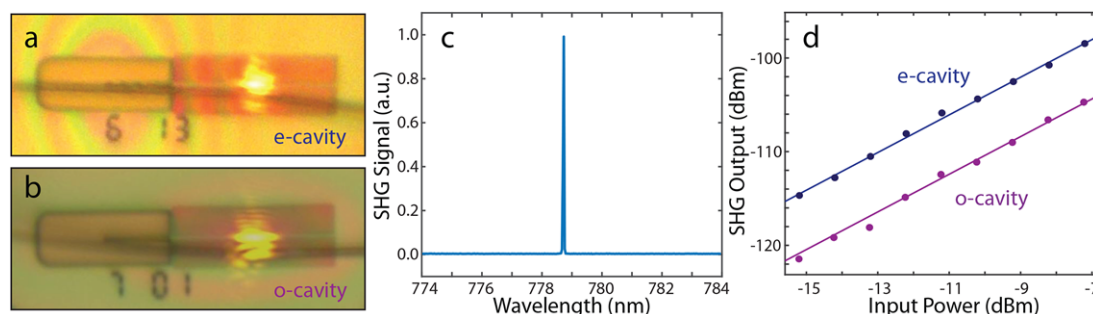


Figure 5. Second-harmonic generation in 2D LN PhC slab nanoresonators. a,b) Optical microscopy images of an e-cavity and o-cavity, respectively, showing bright spots appearing when the pump wave is launched into the cavities. c) Spectrum of generated second harmonic, with a pump wave at 1557.45 nm. d) Recorded power of the generated second-harmonic wave as a function of that of the fundamental pump wave, where the blue and purple dots are experimental recorded data for an e-cavity and o-cavity, respectively. The solid lines show quadratic fitting to the experimental data.

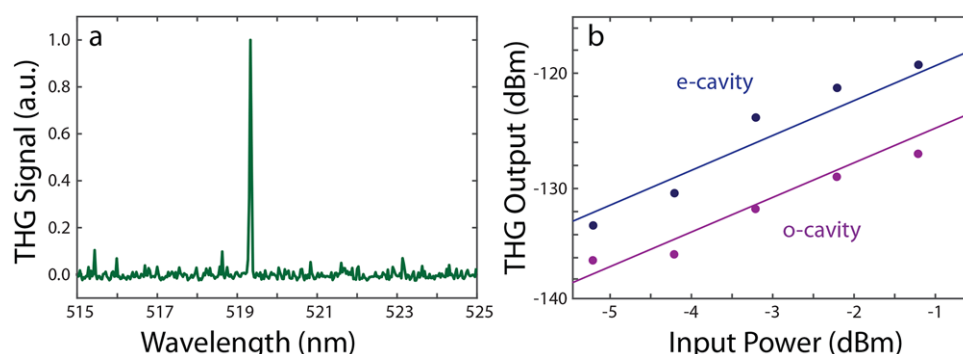


Figure 6. Third-harmonic generation in 2D LN PhC slab nanoresonators. a) Spectrum of the generated third harmonic, with a pump wave at 1557.45 nm. b) Recorded power of the generated third-harmonic wave as a function of the fundamental pump wave, where the blue and purple dots are experimental recorded data for an e-cavity and o-cavity, respectively. The solid lines show cubic fitting to the experimental data.

optimization of the device design and the coupling waveguide would help improve the nonlinear conversion efficiency.

We also characterized the second-harmonic generation in an o-cavity, as shown in Figure 5d. Compared with the e-cavity, the o-cavity exhibits an efficiency about four times lower. It is possibly because the SHG in the e-cavity is dominated by a type-0 process since the cavity field mainly polarizes along the optical axis, while that in the o-cavity is more likely to be a combination of a type-0 and a type-II process since the cavity field is dominantly along the ordinary polarization.

Of particular interest is that the nonlinear optical interaction is enhanced so much in the 2D LN PhC slab nanoresonators that we were even able to observe third-harmonic generation. This is shown in Figure 6, where a clear emission line appears at a wavelength of 519.15 nm, which corresponds directly to the third harmonic of the pump wave at 1557.45 nm. We recorded the power dependence of the third harmonic, which is plotted in Figure 6b. It shows a clear cubic dependence on the pump power, an intrinsic signature of third-harmonic generation. To the best of our knowledge, this is the first time to observe third-harmonic generation in on-chip LN nanophotonic devices.^[15–36] The observed THG could contribute from cascaded SHG, direct THG from the third-order optical nonlinearity, or a combination of these two processes. Similar to the case of the second-harmonic generation, the third-harmonic generation is considerably weaker in the

o-cavity (Figure 6b, purple curve), which is likely due to the tensorial nature of the third-order (and/or second-order) nonlinear susceptibility of lithium niobate.

7. Discussion and Conclusion

We have demonstrated 2D LN PhC slab nanoresonators with optical Q up to 3.51×10^5 that is about three orders of magnitude higher than other 2D LN PhC nanoresonators reported to date.^[37–47] The high optical Q together with tight optical mode confinement results in intriguing nonlinear optical interactions, allowing us to observe both second- and third-harmonic generation.^[15–36] Moreover, the devices exhibit specific polarization of the cavity modes, which enabled us to probe the intriguing anisotropy of nonlinear optical phenomena. We have revealed the peculiar anisotropy of photorefractive quenching and the unique anisotropic thermo-optic nonlinear response.

With the significant optical nonlinearity of lithium niobate material, the demonstrated high-Q 2D LN PhC nanoresonators offer an excellent device platform for exploring extreme nonlinear and quantum optical phenomena in the regime inaccessible to conventional means. For example, the low nonlinear conversion efficiency in our current devices is primarily due to the low optical Q and external coupling at the second and third harmonic.

Therefore, future design to minimize the radiation leakage at the second (and/or third) harmonic frequency would significantly improve the optical Q. Moreover, appropriate design of on-chip coupling waveguide would optimize the external coupling to these wavebands. The resulting device platform would further dramatically enhance nonlinear wave interactions, which would enable exploration of nonlinear and quantum optics at single and few photon levels, which would open up broad nonlinear and quantum photonic applications.^[48]

On the other hand, 2D PhC slab resonators are particularly suitable for optoelectronic integration^[49,50] and for scaling up to large-scale photonic integrated circuits.^[2] As lithium niobate exhibits strong piezoelectric effect, electro-optic effect, and electromechanical coupling, the demonstration of high-Q 2D LN PhC slab nanoresonators thus open the door toward developing large-scale electro-opto-mechanically hybrid integrated LN circuits for broad applications in communication, computing, signal processing, sensing, and energy harvesting.

Acknowledgements

This work was supported in part by the National Science Foundation under Grant Nos. ECCS-1641099, ECCS-1810169, and ECCS-1509749, by the National Institutes of Health under Grant No. R21EB0249988, and by the Defense Advanced Research Projects Agency SCOUT program through Grant No. W31P4Q-15-1-0007 from the U.S. Army Aviation and Missile Research, Development, and Engineering Center (AMRDEC). The views and conclusions contained in this document are those of the authors and should not be interpreted as representing the official policies, either expressed or implied, of the Defense Advanced Research Projects Agency, the U.S. Army, or the U.S. Government. This study was performed in part at the Cornell NanoScale Science and Technology Facility (CNF), a member of the National Nanotechnology Infrastructure Network.

Conflict of Interest

The authors declare no conflict of interest.

Keywords

photonic crystals, lithium niobate, nonlinear optics, integrated optics, photorefractive optics

Received: March 20, 2019
Published online:

- [1] K. Nozaki, T. Tanabe, A. Shinya, S. Matsuo, T. Sato, H. Taniyama, M. Notomi, *Nat. Photonics* **2010**, *4*, 477.
- [2] E. Kuramochi, K. Nozaki, A. Shinya, K. Takeda, T. Sato, S. Matsuo, H. Taniyama, H. Sumikura, M. Notomi, *Nat. Photonics* **2014**, *8*, 474.
- [3] X. Fan, I. M. White, S. I. Shopova, H. Zhu, J. D. Suter, Y. Sun, *Anal. Chim. Acta* **2008**, *620*, 8.
- [4] M. Soljacic, J. D. Joannopoulos, *Nat. Mater.* **2004**, *3*, 211.
- [5] P. Lodahl, S. Mahmoodian, S. Stobbe, *Rev. Mod. Phys.* **2015**, *87*, 347.
- [6] B.-S. Song, S. Noda, T. Asano, Y. Akahane, *Nat. Mater.* **2005**, *4*, 207.
- [7] S. Noda, M. Fujita, T. Asano, *Nat. Photonics* **2007**, *1*, 449.
- [8] S. Combrie, A. De Rossi, Q. Vy Tran, H. Benisty, *Opt. Lett.* **2008**, *33*, 1908.
- [9] B. J. Eggleton, B. Luther-Davies, K. Richardson, *Nat. Photonics* **2011**, *5*, 141.
- [10] N. V. Trivino, M. Minkov, G. Urbinati, M. Galli, J.-F. Carlin, R. Butte, V. Savona, N. Grandjean, *Appl. Phys. Lett.* **2014**, *105*, 231119.
- [11] K. Debnath, M. Clementi, T. D. Bucio, A. Z. Khokhar, M. Sotto, K. M. Grabska, D. Bajoni, M. Galli, S. Saito, F. Y. Gardes, *Opt. Express* **2017**, *25*, 27334.
- [12] M. Kesters, B. Sturman, P. Werheit, D. Haertle, K. Buse, *Nat. Photonics* **2009**, *3*, 510.
- [13] R. S. Weis, T. K. Gaylord, *Appl. Phys. A* **1985**, *37*, 191.
- [14] L. Arizmendi, *Phys. Status Solidi A* **2004**, *201*, 253.
- [15] A. Guarino, G. Poberaj, D. Rezzonico, R. Degl'Innocenti, P. Günter, *Nat. Photonics* **2007**, *1*, 407.
- [16] P. Rabiei, J. Ma, S. Khan, J. Chiles, S. Fathpour, *Opt. Express* **2013**, *21*, 25573.
- [17] L. Chen, Q. Xu, M. G. Wood, R. M. Reano, *Optica* **2014**, *1*, 112.
- [18] C. Wang, M. J. Burek, Z. Lin, H. A. Atikian, V. Venkataraman, I.-C. Huang, P. Stark, M. Lončar, *Opt. Express* **2014**, *22*, 30924.
- [19] J. Lin, Y. Xu, Z. Fang, M. Wang, J. Song, N. Wang, L. Qiao, W. Fang, Y. Cheng, *Sci. Rep.* **2015**, *5*, 8072.
- [20] R. Geiss, S. Saravi, A. Sergeev, S. Diziain, F. Setzpfandt, F. Schrempel, R. Grange, E.-B. Kley, A. Tünnermann, T. Pertsch, *Opt. Lett.* **2015**, *40*, 2715.
- [21] J. Wang, F. Bo, S. Wan, W. Li, F. Gao, J. Li, G. Zhang, J. Xu, *Opt. Express* **2015**, *23*, 23072.
- [22] S. Li, L. Cai, Y. Wang, Y. Jiang, H. Hu, *Opt. Express* **2015**, *23*, 24212.
- [23] P. O. Weigel, M. Savanier, C. T. DeRose, A. T. Pomerene, A. L. Starbuck, A. L. Lentine, V. Stenger, S. Mookherjee, *Sci. Rep.* **2016**, *6*, 22301.
- [24] W. C. Jiang, Q. Lin, *Sci. Rep.* **2016**, *6*, 36920.
- [25] L. Chang, Y. Li, N. Volet, L. Wang, J. Peters, J. E. Bowers, *Optica* **2016**, *3*, 531.
- [26] A. Rao, J. Chiles, S. Khan, S. Toroghi, M. Malinowski, G. F. Camacho-González, S. Fathpour, *Appl. Phys. Lett.* **2017**, *110*, 111109.
- [27] C. Wang, X. Xiong, N. Andrade, V. Venkataraman, X.-F. Ren, G.-C. Guo, M. Lončar, *Opt. Express* **2017**, *25*, 6963.
- [28] R. Luo, H. Jiang, H. Liang, Y. Chen, Q. Lin, *Opt. Lett.* **2017**, *42*, 1281.
- [29] X. Sun, H. Liang, R. Luo, W. C. Jiang, X.-C. Zhang, Q. Lin, *Opt. Express* **2017**, *25*, 13504.
- [30] J. D. Witmer, J. A. Valery, P. Arrangoiz-Arriola, C. J. Sarabalis, J. T. Hill, A. H. Safavi-Naeini, *Sci. Rep.* **2017**, *7*, 46313.
- [31] R. Luo, H. Jiang, S. Rogers, H. Liang, Y. He, Q. Lin, *Opt. Express* **2017**, *25*, 24531.
- [32] H. Liang, R. Luo, Y. He, H. Jiang, Q. Lin, *Optica* **2017**, *4*, 1251.
- [33] R. Wolf, I. Breunig, H. Zappe, K. Buse, *Opt. Express* **2017**, *25*, 29927.
- [34] C. Wang, Z. Li, M.-H. Kim, X. Xiong, X.-F. Ren, G.-C. Guo, N. Yu, M. Lončar, *Nat. Commun.* **2017**, *8*, 2098.
- [35] I. Krasnokutskaya, J.-L. J. Tambasco, X. Li, A. Peruzzo, *Opt. Express* **2018**, *26*, 897.
- [36] C. Wang, M. Zhang, B. Stern, M. Lipson, M. Lončar, *Opt. Express* **2018**, *26*, 1547.
- [37] M. Roussey, M.-P. Bernal, N. Courjal, F. I. Baida, *Appl. Phys. Lett.* **2005**, *87*, 241101.
- [38] G. Zhou, M. Gu, *Opt. Lett.* **2006**, *31*, 2783.
- [39] M. Roussey, M.-P. Bernal, N. Courjal, D. Van Labeke, F. I. Baida, R. Salut, *Appl. Phys. Lett.* **2006**, *89*, 241110.
- [40] F. Sulser, G. Poberaj, M. Koechlin, P. Günter, *Opt. Express* **2009**, *17*, 20291.
- [41] R. Geiss, S. Diziain, R. Iliew, C. Etrich, H. Hartung, N. Janunts, F. Schrempel, F. Lederer, T. Pertsch, E.-B. Kley, *Appl. Phys. Lett.* **2010**, *97*, 131109.
- [42] N. Courjal, S. Benhabane, J. Dahdah, G. Ulliac, Y. Gruson, V. Laude, *Appl. Phys. Lett.* **2010**, *96*, 131103.

- [43] N. Courjal, J. Dahdah, G. Ulliac, P. Sevilano, B. Guichardaz, F. Baida, *Opt. Express* **2011**, 19, 23008.
- [44] H. Lu, F. I. Baida, G. Ulliac, N. Courjal, M. Collet, M.-P. Bernal, *Appl. Phys. Lett.* **2012**, 101, 151117.
- [45] S. Diziain, R. Geiss, M. Zilk, F. Schrepel, E.-B. Kley, A. Tünnermann, T. Pertsch, *Appl. Phys. Lett.* **2013**, 103, 051117.
- [46] R. Geiss, S. Diziain, M. Steinert, F. Schrepel, E.-B. Kley, A. Tünnermann, T. Pertsch, *Phys. Stat. Sol. A* **2014**, 211, 2421.
- [47] L. Cai, H. Han, S. Zhang, H. Hu, K. Wang, *Opt. Lett.* **2014**, 39, 2094.
- [48] D. E. Chang, V. Vuletic, M. D. Lukin, *Nat. Photonics* **2014**, 8, 685.
- [49] M. Winger, T. D. Blasius, T. P. M. Alegre, A. H. Safavi-Naeini, S. Meenehan, J. Cohen, S. Stobbe, O. Painter, *Opt. Express* **2011**, 19, 24905.
- [50] H. C. Nguyen, S. Hashimoto, M. Shinkawa, T. Baba, *Opt. Express* **2012**, 20, 22465.